

MSc PHYSICS

Gravitation, Astro- and Particle Physics

MASTER'S THESIS

Determining the Sources of Cosmic Neutrinos

by

Bas Johannes Jan Jongewaard BSc

10375457

July 24, 2017

60 ECTS

supervisor:

Dr. A.J. HEIJBOER

second examiner:

Dr. S. ANDO



Contents

1	Introduction	3
2	Cosmic Neutrinos	4
2.1	History	4
2.2	The Standard Model	6
2.3	Source Candidates	8
3	KM3NeT	11
3.1	Cosmic Rays	12
3.2	Cherenkov Radiation	14
3.3	Detection	15
4	Neutrino Sources in the Universe	17
4.1	Distance Measures	17
4.2	Amount of Neutrino Sources	18
4.3	Neutrino Flux	20
4.4	Simulating a Universe of Neutrino Source Candidates	21
5	Simulation of the Expected Signal	23
5.1	Sky Maps	23
5.2	Counting Hits	24
5.3	Confidence Levels	26
6	Analysis	27
6.1	Source Distribution	27
6.2	Flux Distribution	29
6.3	Benchmark Significance	30
6.4	Different Detector Models	32
7	Conclusions and Outlook	36
7.1	Conclusions	37
	Bibliography	38

CONTENTS	2
List of Figures	40
List of Tables	43
Acknowledgements	44

Abstract

KM3NeT is a future European large-volume deep-sea neutrino telescope that will search for neutrinos of cosmic origin. Recent studies by IceCube have confirmed their existence, but have not been able to identify their sources. Several source candidates have been suggested, of which blazars, hard X-ray emitting active galactic nuclei (AGN) and starburst galaxies have been considered in this research. For each of these sources, the statistical sensitivity of an analysis which compares the arrival direction of neutrinos to a catalogue of source objects has been investigated. It is assumed that the distribution of each source class throughout the Universe as a function of redshift follows the star formation rate (SFR), multiplied by their local source density \mathcal{H}_0 . Furthermore, it is assumed that all sources of a given type are standard candles. Lastly, we will make the bold assumption that ‘perfect’ catalogues are available for any source type. Using these assumptions, plus the total flux observed by IceCube, source distributions and corresponding flux distributions will be computed. These distributions are subsequently used to model the signal, for different values of two main parameters: the number of detected neutrinos N_ν and angular resolution ψ of the detector. We will investigate the dependence of the significance on these parameters. The modelled signals will subsequently be compared to the catalogues. It is concluded that a small resolution is a hard requirement to achieve high confidence levels, especially for source candidates with a relatively high local source density. However, it follows that a worse resolution can be compensated by a better acceptance. For higher local source densities, $N_\nu \rightarrow \alpha N_\nu$ has approximately the same effect on the significance as $\psi \rightarrow \psi/\alpha$. We should be able to test the hypotheses on source candidates, as the confidence levels are all above 3σ , provided we measure long enough.

Chapter 1

Introduction

KM3NeT is a future European neutrino telescope that will be located at the bottom of the Mediterranean Sea. It will search for neutrinos from distant objects in the Universe. In 2013 [1], the IceCube experiment discovered neutrinos of cosmic origin, but has been unable to determine their sources so far. If these cosmic neutrino sources can be found, it will allow physicists to observe cosmological objects in a new way and to study particle physics at energies up to the PeV scale.

The current goal is to discover what kind of astrophysical objects are responsible for the production of the ‘IceCube neutrinos’. Several source candidates have been suggested, like various types of Active Galactic Nuclei (such as blazars), starburst galaxies and galaxy clusters [2; 3; 4]. The best way to test these hypotheses is to compare the direction of the detected neutrinos to sources in a catalogue, and search for matches.

This method is expected to greatly benefit from an improved detector, which is where KM3NeT comes in. This research project will investigate the importance of the pointing resolution of the KM3NeT detector when searching for cosmic neutrino sources. Furthermore, the role of this resolution versus the detector’s acceptance (i.e. its effective surface area, the amount of neutrinos detected in a given time interval) is explored. Another interesting question is whether the detector can detect cosmic neutrinos with a sufficiently high significance to test the various hypotheses about potential neutrino sources.

To find answers to these questions, this thesis will first elaborate on the relevant theory on cosmic neutrinos and the KM3NeT experiment, in sections 2 and 3. Subsequently, populations of source candidates will be simulated in section 4, with the main difference between different source candidates being their abundance in the Universe. The obtained source distributions and corresponding flux distributions will then be used in section 5 to predict the obtained signal for different detector and model parameters. The results will be analysed in section 6, resulting in answers to the research questions specified above, as well as some recommendations for future studies, which will both be discussed in section 7.

Chapter 2

Cosmic Neutrinos

Neutrinos are of key importance to astrophysics. As neutrinos barely interact with any other form of matter, they pass right through almost everything in their path. Moreover, they are not deflected by magnetic fields, due to a lack of electric charge. Therefore, when detected, nearly all of the neutrinos will have been coming directly from their source, without any deviations. This means that the source should be located in exactly the same direction as the neutrino was coming from. This will allow physicists to identify and better understand the sources of cosmic neutrinos.

In this section, it is explained what neutrinos are and how they were first discovered. An overview of the Standard Model of particle physics is given, which helps to demonstrate why the neutrino hardly interacts with other matter. Moreover, the concept of cosmic neutrinos is addressed and the major source candidates considered in this study are listed and examined in detail.

2.1 History

Back in the 1920s, the general consensus amongst physicists was that all matter was composed of protons and electrons. Moreover, the universe was thought to be isotropic and homogeneous, thanks to symmetries and conservation laws [5].

Beta decay, however, posed a serious problem. In this radioactive decay, an electron (or a positron) is emitted from the nucleus of an atom, whilst changing the element by converting a neutron into a proton (or vice versa):

$$n \rightarrow p + e^- \tag{2.1}$$

It follows that after the interaction, we are - seemingly - left with the electron and the recoiling daughter nucleus.

If we now assume the parent nucleus was at rest and decompose the particles' energies in terms of rest energy (mc^2) and kinetic energy (T), energy and momentum conservation will give us the following equation for the kinetic energy of the final electron:

$$T_e = \Delta m c^2 - T_{\text{daughter}} \approx \Delta m c^2 \quad (2.2)$$

Consequently, we can conclude that if beta decay is a two-body decay, the emitted electrons will have a kinetic energy equal to approximately $T_e = \Delta m c^2$, which is constant for a given decay [6].

Experiments, however, showed that the emitted electrons had a continuous energy spectrum, up to a maximum energy $T_{\text{max}} = \Delta m c^2$ (see figure 2.1).

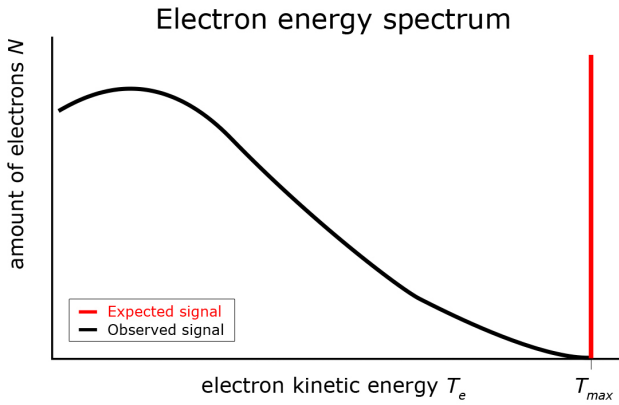


Figure 2.1: For a two-body decay, all observed electrons are expected to have the same energy $T_e = \Delta m c^2$ (the red line). The black curve shows the observed spectrum. Note that the amount of electrons converges to zero at $T_e = T_{\text{max}} = \Delta m c^2$. Figure originally taken from [7].

This would imply that energy is not conserved in these decays. Moreover, since electrons, protons and neutrons all have spin-1/2 (see section 2.2), angular momentum would not be conserved either. As a result, through Noether's Theorem - for any conserved quantity, there exists an underlying symmetry - this would mean the universe is not isotropic and not homogeneous.

A different explanation, provided by Wolfgang Pauli in 1930, is that an additional particle was produced, carrying away a part of the energy. To conserve angular momentum, the particle would have to have spin 1/2. Furthermore, to conserve charge, the particle had to be neutral, which could also explain why the particle had not been detected [6].

In 1956, this particle, called the **neutrino** ('little neutral one'), was discovered by Cowan and Reines [8].

2.2 The Standard Model

Nowadays, the leading theory in particle physics is the Standard Model (SM). It lists all known fundamental particles and describes three of the four fundamental forces in nature: the electromagnetic, weak and strong interactions. Moreover, it explains the mechanism by which particles acquire mass.

All fundamental particles in the model can be classified as either fermions (half-integer spin) or bosons (integer spin). The set of fundamental fermions, which all have spin-1/2, consists of 6 quarks and 6 leptons. The u , c and t quarks are called ‘up-type’ quarks and have charge +2/3, whereas the d , s and b quarks are called ‘down-type’ quarks and have charge -1/3. Moreover, all quarks carry colour charge. The leptons can be divided into the charged leptons e , μ and τ , and their corresponding neutrinos ν_e , ν_μ and ν_τ . The charged leptons all have electromagnetic charge -1, the neutrinos are neutral. The leptons do not carry any colour charge [9]. Figure 2.2 lists all fundamental particles in the Standard Model, including their mass, charge and spin.

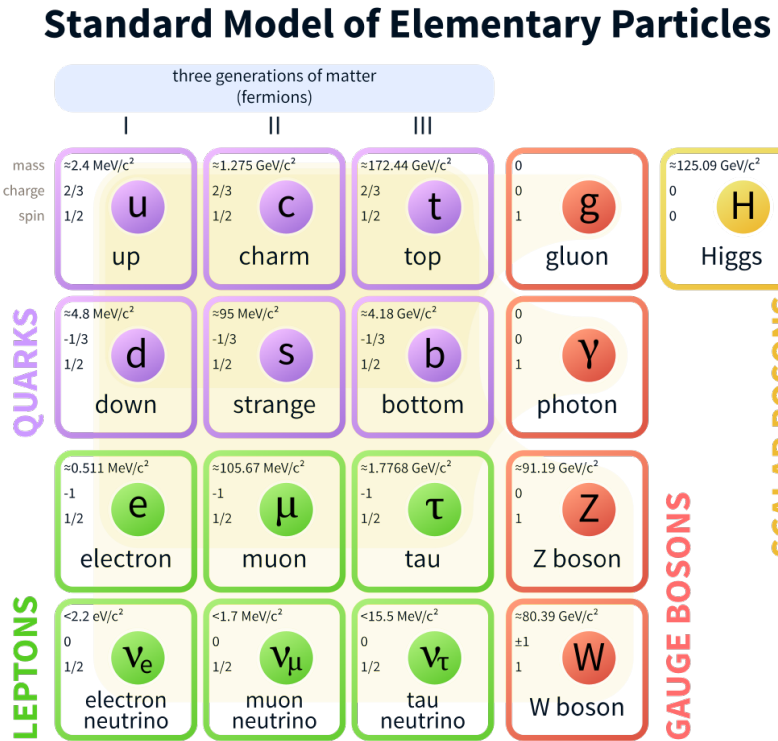


Figure 2.2: Summary of all fundamental particles in the Standard Model. The first three columns contain the fermions, particles with half-integer spin. The quarks are in purple, the leptons in green. The fourth column lists the gauge bosons, particles with integer spin that act as mediators of the fundamental interactions. On the top right in yellow is the Higgs boson, which provides the mechanism by which particles acquire mass.

According to the Standard Model, particles interact with each other by exchanging a so-called gauge boson (or force carrier). These gauge bosons, all spin-1, are the massless photon γ and gluon g , and the massive W^\pm and Z bosons. The photon is the mediator of the electromagnetic interaction. Since it couples to charge, it can interact with all fundamental fermions, except for the neutrinos. Furthermore, it can interact with the charged W^\pm boson. The strong force is mediated by gluons, which couple to colour charge. Since colour charge is carried solely by quarks and the gluons themselves, these are the only particles than can interact strongly. Finally, the massive W^\pm and Z bosons are responsible for the charged-current and neutral-current weak interactions. They couple to all fundamental fermions. The W^\pm boson changes the flavour of the fermion, the Z does not [9].

In addition, the Standard Model includes the Higgs boson H , a spin-0 boson which gives mass to the other particles in the model and to itself. It was discovered in 2012 at CERN by the ATLAS and CMS collaborations [10; 11].

An overview of all interactions in the Standard Model can be found in figure 2.3. Clearly, the neutrinos do not couple to the photon, gluon and quarks. This explains why neutrinos are so hard to detect: they only couple to other leptons and the W^\pm and Z bosons (and presumably to the Higgs boson, provided they have a nonzero mass).

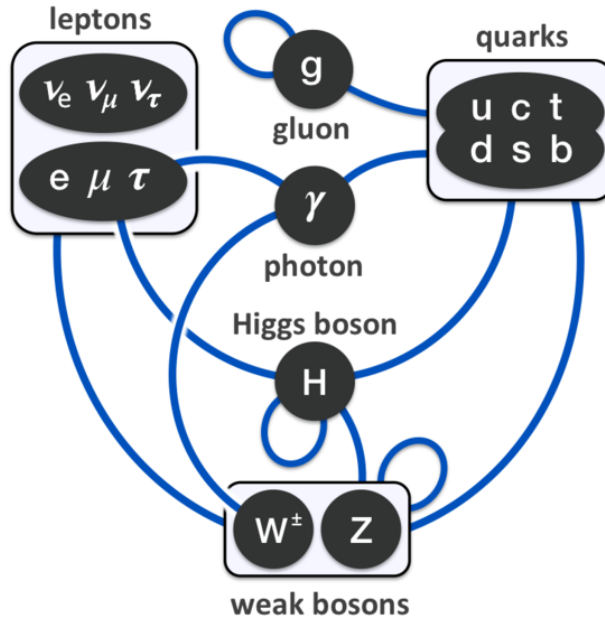


Figure 2.3: Graphical overview of the interactions in the Standard Model. The interactions are indicated by blue lines, the elementary particles by the black dots. As shown, the gluon only interacts with the colour-carrying quarks, the photon couples to all quarks, the charged leptons and W^\pm boson, the weak gauge bosons to all quarks and leptons and the Higgs boson to all particles that have mass, including itself. Note that this graph assumes the neutrinos to be massless (and therefore assumes that there exist no interactions between neutrinos and the Higgs boson).

2.3 Source Candidates

In 2013, the IceCube Neutrino Observatory presented the first-ever evidence for high-energy neutrinos of cosmic origin [1]. The isotropy of the signal suggests the neutrinos are of extra-galactic origin. Their exact origin, however, still remains unknown, since IceCube’s angular resolution is not small enough to point the signal back to individual sources. Naturally, the significance with which the individual sources can be identified is coupled strongly to the amount of sources as well. A better resolution is always valuable, but the lack of correlation with existing source catalogues indicates that there are a great many sources. The major candidates for cosmic neutrino sources considered in this study are starburst galaxies, active galactic nuclei and blazars [3]. The last part of this section will outline their main characteristics.

Starburst Galaxies

Starburst galaxies are galaxies with a relatively high star formation rate. This higher rate is caused by the high average gas density in the centre of the galaxy, which, in turn, is usually caused by a merger of multiple galaxies. The produced stars are relatively massive and will quickly burn up, producing supernovae, leading to additional star formation [12]. Acceleration processes in supernova remnant shocks produce cosmic rays, which are confined within the galaxy by a strong magnetic field. Consequently, the interactions leading to neutrinos occur within the starburst galaxy, after which the neutrinos, being insensitive to magnetic fields, are able to propagate through the Universe [13]. The Antennae Galaxies, two known starburst galaxies, are shown in figure 2.4.



Figure 2.4: The Antennae Galaxies (NGC 4038 and NGC 4039), two interacting galaxies currently going through a starburst phase. The collision of the two galaxies causes a very high star formation [14].

Active Galactic Nuclei

Active galactic nuclei (AGN) are massive black holes ($\sim 10^8 M_\odot$) at the centre of galaxies with a relatively high luminosity. The accretion of matter from the galaxy onto the black hole produces cosmic rays in two relativistic jets and causes shock fronts, which accelerate the produced protons, making them interact with other particles to form highly energetic pions. These pions will decay during flight and, as described in section 3.1, produce neutrinos and charged leptons [15]. See figure 2.5 for a graphical summary of AGN. In this research, only hard X-ray emitting AGN will be considered.

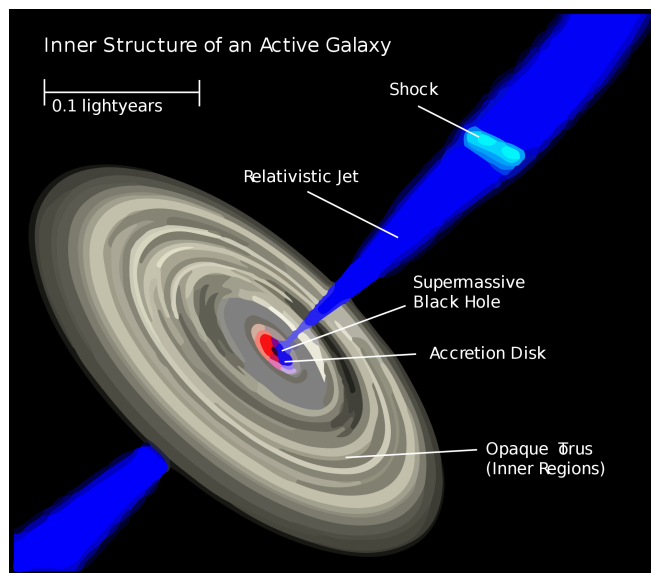


Figure 2.5: Image of a galaxy with an active galactic nucleus. The nucleus, a (super)massive black hole (shown in red), accretes matter from the galaxy (grey disk), producing relativistic jets of particles in the process (dark blue). The accretion process causes shock fronts (light blue) as well, accelerating the particles in the jets. These particles interact with other particles and form pions, which eventually decay to neutrinos during flight.

Blazars

Blazars are an extreme class of AGN, having supermassive black holes at their centre. They are among the most luminous phenomena in the Universe, presumably because their relativistic jets (approximately) face our direction. This feature makes them scarcer than other types of AGN [16].

In this research, we will distinguish the different types of source by their local source density only. As we will see later, the local source density is a main parameter that will determine the power of catalogue searches. Table 2.1 shows typical local source densities for the source candidates mentioned above: the typical amount of source candidates per unit volume, at a redshift of $z = 0$.

Class of source	Local source density (Mpc^{-3})
Starburst galaxies	10^{-4}
Hard X-ray emitting AGN	10^{-6}
Blazars	10^{-9}

Table 2.1: Typical - but approximate - numbers for the local source densities of the different source candidates considered in this project: starburst galaxies, hard X-ray emitting AGN and blazars [3; 4; 2].

Chapter 3

KM3NeT

KM3NeT - an acronym for Cubic Kilometre Neutrino Telescope - is a European research infrastructure situated at three locations in the Mediterranean Sea: Toulon in France, Capo Passero in Italy and eventually Pylos in Greece (see figure 3.1). These sites will house the next generation of neutrino telescopes that will have detector volumes of several cubic kilometres of sea water [17].

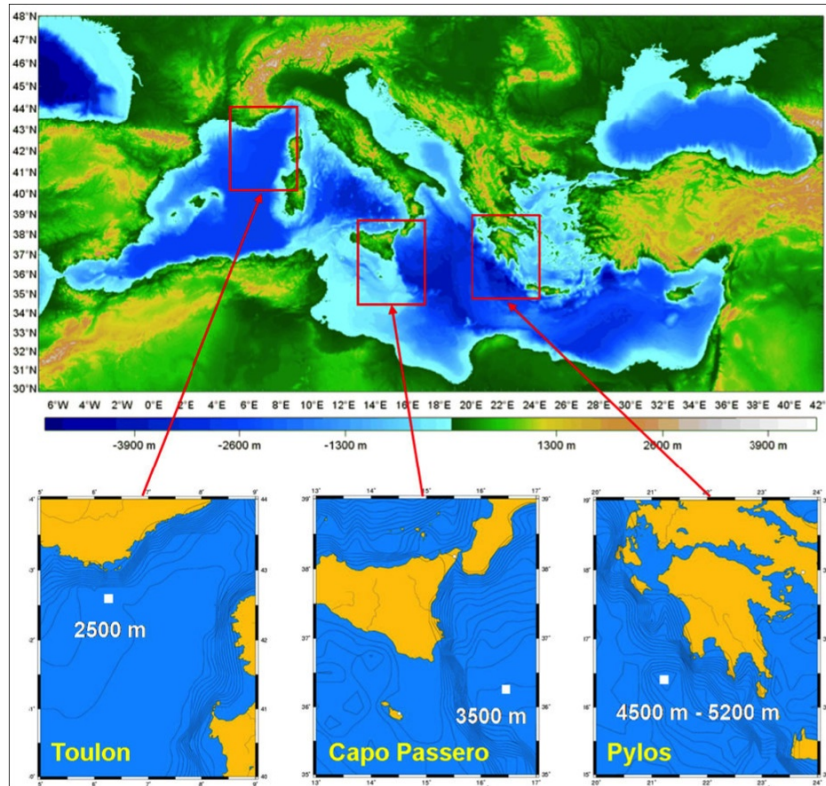


Figure 3.1: Map of the Mediterranean Sea showing the locations of the three KM3NeT sites: Toulon (France), Capo Passero (Italy) and Pylos (Greece) [18].

KM3NeT has two main objectives: the discovery and subsequent observation of (extragalactic) high-energy neutrino sources in the Universe, and the determination of the mass hierarchy of neutrinos. These goals are greatly motivated by two recent significant discoveries: the high-energy cosmic neutrino signal reported by the IceCube experiment and the large contribution of electron neutrinos to the third neutrino mass eigenstate [19].

KM3NeT consists of two main detectors: Oscillation & Astrophysical Research with Cosmics in the Abyss (ORCA & ARCA). ARCA will focus on the first objective: the detection of high-energy cosmic neutrinos and identifying their sources. ORCA, on the other hand, will measure atmospheric neutrino oscillation parameters, to determine the neutrino mass hierarchy. Furthermore, ORCA will be able to observe low-mass dark matter and, possibly, the composition of the Earth’s interior as well, through neutrino tomography [20].

As discussed, KM3NeT will focus on detecting both cosmic and atmospheric neutrinos. This study will only take cosmic neutrinos into account, and neglect any effects caused by atmospheric neutrinos. It is still convenient, however, to have an insight in the concept of atmospheric neutrinos and how they are produced, since they will unavoidably cause background noise in real data. Therefore, this section will briefly outline the concept of cosmic rays first. Furthermore, this section will explain Cherenkov radiation: the mechanism by which neutrinos can be detected in KM3NeT. Finally, the hardware that detects the Cherenkov radiation is described.

3.1 Cosmic Rays

The Earth’s atmosphere is continually being ‘bombarded’ by relativistic, (frequently) charged particles, originating from the Sun and sources outside our solar system, such as galaxies and supernovae. The existence of these cosmic rays was first discovered by Victor Hess in 1912 during a balloon flight. At energies above a few TeV, cosmic rays are not being deflected by magnetic fields, resulting in an isotropic distribution [15].

Cosmic rays are mainly composed of protons ($\sim 84\%$) and alpha particles ($\sim 10\%$). The remainder consists of heavier nuclei, electrons and positrons [21]. When these rays, primarily composed of protons, enter the Earth’s atmosphere, we get the following main reactions:

$$\begin{aligned} p + p &\longrightarrow p + n + \pi^+ \\ p + p &\longrightarrow p + p + \pi^0 \\ p + n &\longrightarrow n + n + \pi^+ \\ p + n &\longrightarrow p + n + \pi^0 \\ p + n &\longrightarrow p + p + \pi^- \end{aligned} \tag{3.1}$$

Since the mean lifetime of both charged and neutral pions is very short (26 ns and 10^{-16} s respectively), the pions typically do not interact before decaying [22]. As a result, their decay

products can be very energetic. Neutral pions decay to two photons, whereas charged pions decay to a muon and its corresponding (atmospheric) neutrino:

$$\begin{aligned}\pi^- &\rightarrow \mu^- + \bar{\nu}_\mu \\ \pi^+ &\rightarrow \mu^+ + \nu_\mu \\ \pi^0 &\rightarrow \gamma + \gamma\end{aligned}\tag{3.2}$$

The photons will create an electromagnetic shower of electrons and photons: the photons will produce electron-positron pairs, which will subsequently lose energy by mechanisms like bremsstrahlung. See figure 3.2 for an overview of a cosmic ray in the Earth's atmosphere.

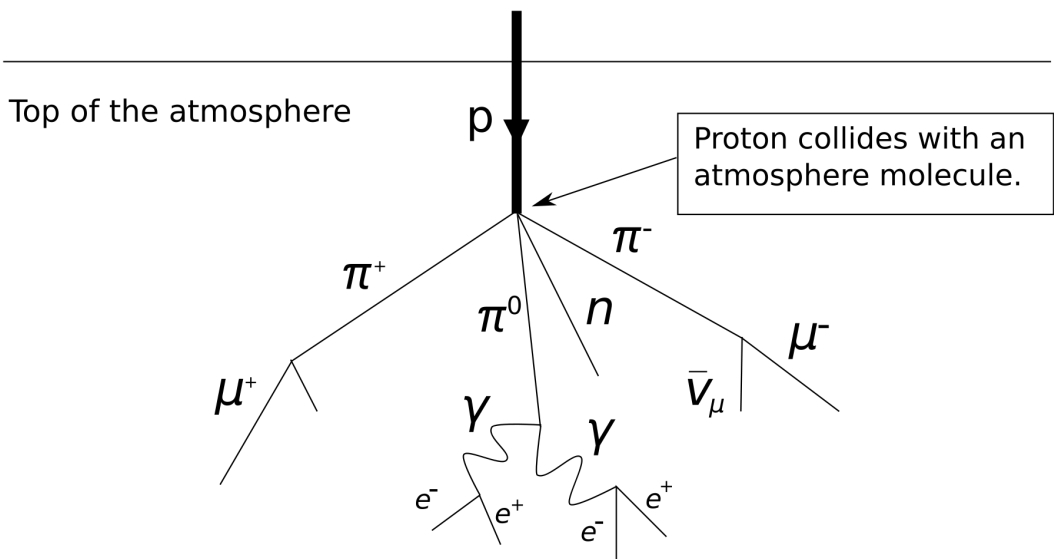


Figure 3.2: Schematic of the main interactions of cosmic rays in the Earth's atmosphere. Protons enter the atmosphere and collide with atmosphere molecules. The main products of these interactions are pions, neutrons and protons. The neutral pions decay to two photons, starting an electromagnetic cascade of photons and electrons. The charged pions, on the other hand, will decay to (anti)muons and their corresponding (anti)neutrinos.

Since the neutrinos in equation set 3.2 barely interact with other matter, they will go right through the Earth. Some of them, however, will eventually interact with other matter by exchanging a W boson, resulting in a muon [22; 23].

If this interaction occurs on the other side of the Earth, the resulting muon can be detected and differentiated from the muons produced in pion decay, as the muon is going upward in the detector, whilst the muons in equation set 3.2 are going downward.

3.2 Cherenkov Radiation

As explained in chapter 2.2, neutrinos barely interact with other matter, making them almost impossible to detect directly. High-energy neutrinos, however, can interact with matter to produce relativistic charged particles, which will emit Cherenkov radiation as they traverse the water. This radiation can be detected with detection units (see section 3.3). In this section, the physics involved in Cherenkov radiation will be addressed.

When a charged particle propagates through vacuum with constant velocity, it will not emit any radiation. However, if it traverses a dielectric medium with refractive index $n > 1$, the particle polarises the molecules in the medium. When the particle has passed, the molecules fall back into their unpolarised state, by emitting a photon. If the velocity of the charged particle is greater than the speed of light in the medium ($v > \frac{c}{n}$, or $\beta > \frac{1}{n}$), constructive interference will occur and the photons will be emitted as Cherenkov radiation [9]. A graphical overview is given in figure 3.3.

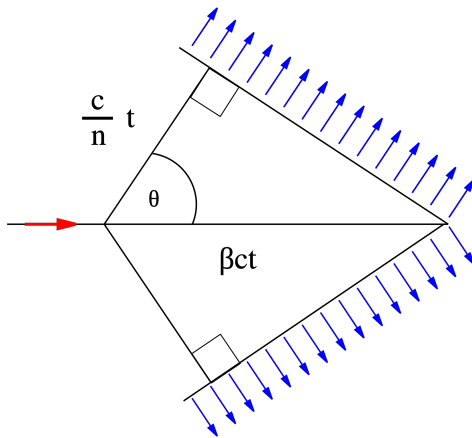


Figure 3.3: Schematic of Cherenkov radiation. An incoming charged particle, depicted by the red arrow, traverses a dielectric medium with refractive index n at velocity $v = \beta c$. If $\beta > \frac{1}{n}$, constructive interference will occur and Cherenkov radiation will be emitted (blue arrows).

A remarkable feature of Cherenkov radiation is that the angle θ between the charged particle and the emitted photon depends only on the velocity of the particle and the refractive index of the medium:

$$\cos \theta = \frac{1}{\beta n} \quad (3.3)$$

For relativistic velocities, $\beta \approx 1$, meaning that the angle will depend on n alone. For water, the refractive index is given by $n = 1.35$, resulting in a constant angle of approximately $\theta \approx 42^\circ$. This known and constant angle can be used to reconstruct the tracks of the charged particles.

3.3 Detection

The Cherenkov radiation emitted by relativistic muons will be detected by photo-sensors, which will be encased, together with read-out electronics, within pressure-resistant glass spheres, the so-called Digital Optical Modules (DOMs). The DOMs will be attached to flexible strings, that are attached to the seabed and held upright by submerged buoys. All three ‘building blocks’ of KM3NeT will contain 115 detection strings, which are about 700 metres in height each. Every detection unit hosts 18 DOMs [19]. See figure 3.4 for a graphical impression of a KM3NeT building block.

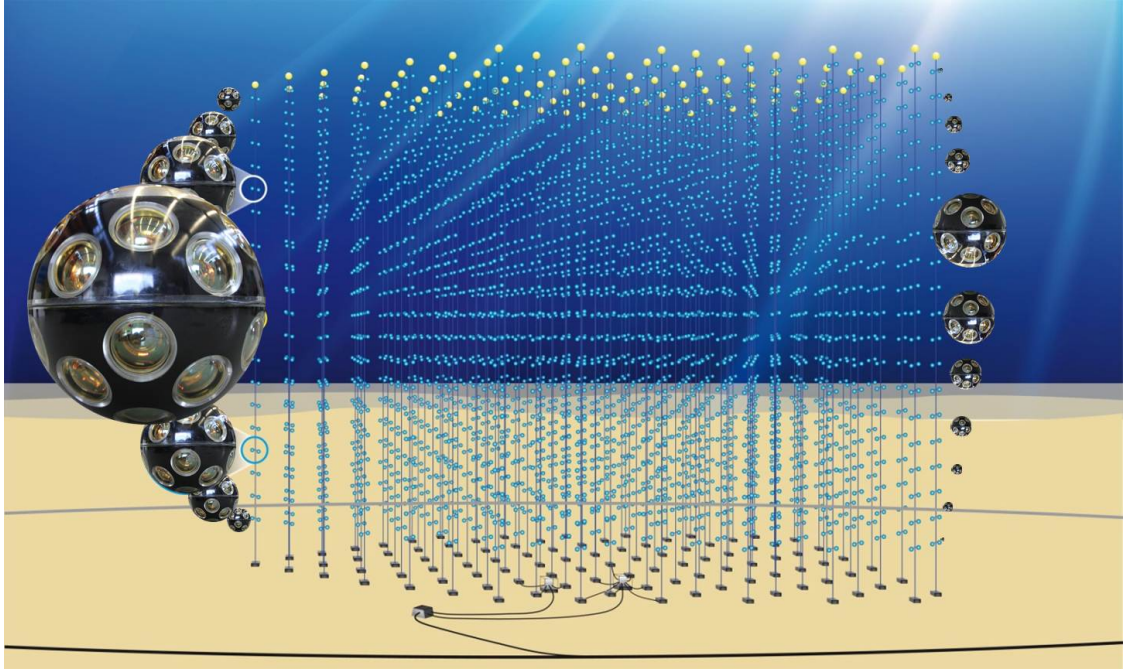


Figure 3.4: Schematic overview of a KM3NeT building block [17].

Each DOM is 17 inches in diameter and contains 31 photomultiplier tubes (PMTs) that detect the incoming Cherenkov light. The PMTs are distributed over the DOM in 5 rings of 6 PMTs, plus one PMT at the bottom pointing downwards, to maximise the coverage. The directional information of this setup enables an improved rejection of noise as well. The positions of the PMTs are fixed by placing them in a 3D-printed support structure. A reflection ring around the face of each PMT improves the photon collection efficiency by 20-40%. Optical contact is assured by filling cavities between the support structure and the glass with an optical gel. The readout electronics are located at the centre of the DOM [19; 24]. Figure 3.5 shows a fully assembled DOM.



Figure 3.5: Photograph of a Digital Optical Module (DOM). The yellow disks are the faces of the photomultiplier tubes [19].

The photomultiplier tubes measure 3 inches in diameter [24] and have three main components: the photocathode, the anode, and the dynodes (or electron multipliers) in between. If incident photons hit the photocathode, (photo)electrons are emitted from the material through the photoelectric effect. By using electric fields, the produced electrons are directed towards the first dynode, where they are multiplied. Every consecutive dynode is kept at an increased voltage with respect to the previous one, to create a voltage gradient and therefore a net electric field, directing the electrons towards the anode. The electrons are collected at the anode, where they induce a current [25]. See figure 3.6 for a schematic overview.

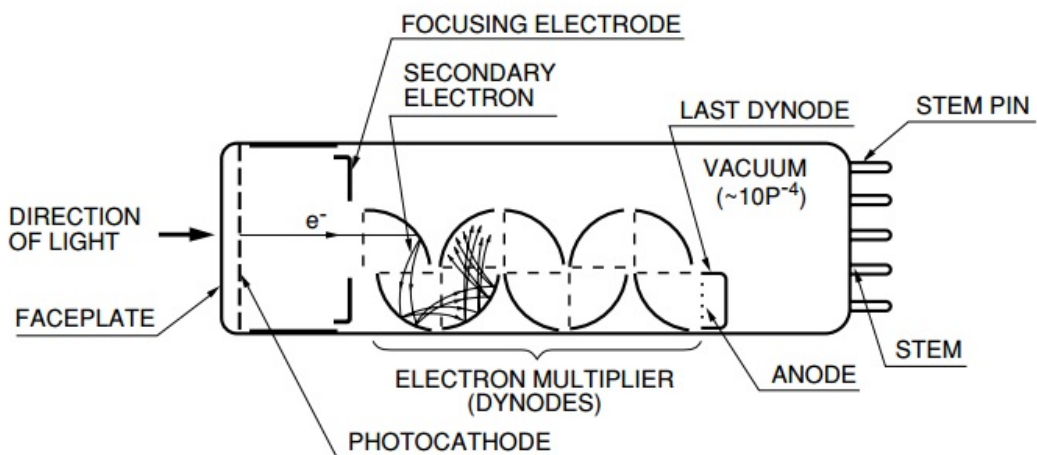


Figure 3.6: Illustration of a photomultiplier tube (PMT). On the left, photons strike the photocathode, producing electrons. The electrons are directed to the dynodes using an electric field. At every dynode, the amount of electrons is multiplied. Eventually, the electrons are collected at the anode, where they induce a current [25].

Chapter 4

Neutrino Sources in the Universe

To determine the sources of cosmic neutrinos, we will eventually compare our signal to catalogues of source candidates. In order to optimise the detector performance, a deep understanding of the source and flux distributions in a ‘perfect’ catalogue is required. In this section, the necessary theory on cosmological distance measures is elaborated upon, after which relations for the distribution of source candidates in the Universe and their flux will be derived. This allows us to simulate a perfect catalogue, up to a given redshift.

To simplify the simulation, several assumptions have been made. We assume that our signal is perfectly isotropic, as is our detection coverage. In addition, we assume that the neutrino flux as observed on Earth consists of our cosmic neutrinos only, and we neglect the effects of atmospheric neutrinos.

4.1 Distance Measures

Since cosmic neutrinos can reach us from cosmological distances ($z \gg 1$), we have to take the expansion of the Universe into account when simulating the source candidates. In order to do so, we follow [26] and make use of the **co-moving distance**, which factors out the expanding Universe, thus remaining constant in time and independent of the observer’s location [27]. Assuming that we live in a flat Universe, the co-moving distance D_C is given as a function of the redshift z by

$$D_M(z) = D_C(z) = D_H \int_0^z \frac{dz'}{E(z')} \quad (4.1)$$

where D_H is the Hubble distance ($= c/H_0$). $E(z)$ is defined as

$$E(z) \equiv \sqrt{\Omega_M(1+z)^3 + \Omega_k(1+z)^2 + \Omega_\Lambda} = \frac{H(z)}{H_0} \quad (4.2)$$

where Ω_M , Ω_k and Ω_Λ are the so-called density parameters of matter, curvature and the cosmological constant at the present moment, H_0 is the Hubble constant ($= 67.6 \text{ km s}^{-1}$

Mpc^{-3}) and $H(z)$ is the Hubble parameter. For our assumed flat Universe, $\Omega_M = 0.3089$, $\Omega_\Lambda = 0.6911$ and $\Omega_k = 0$. The co-moving distance D_C is plotted as a function of redshift in figure 4.1.

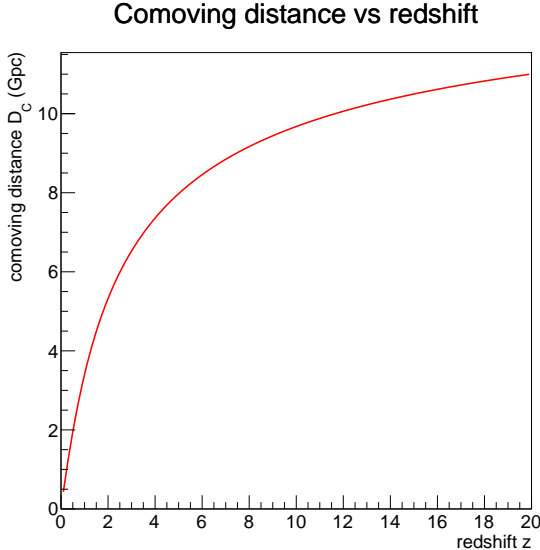


Figure 4.1: Graph showing the co-moving distance D_C corresponding to a redshift z . Redshift is a dimensionless quantity, co-moving distance is given in Gpc.

An infinitesimally thin shell of **co-moving volume** V_C is given by

$$dV_C = D_H \frac{D_C^2(z)}{E(z)} d\Omega dz \quad (4.3)$$

where integrating over $d\Omega$ and dividing by dz gives

$$\frac{dV_C}{dz} = 4\pi D_H D_C^2(z) \frac{1}{E(z)} \quad (4.4)$$

4.2 Amount of Neutrino Sources

As discussed earlier, cosmic neutrinos can reach us from cosmological distances, corresponding to redshifts of $z \gg 1$. This means that, apart from the expansion, we also have to take into account the time-evolution of the Universe. Due to the finite speed of light, looking further away implies looking back in time. Since certain objects can have different abundances at different cosmological times, source distributions can vary with redshift. This redshift dependence is expressed in so-called **evolution functions**, giving the amount of sources per unit co-moving volume.

Like Ahlers and Halzen in [3], we will assume that the distribution of all neutrino source candidates in the Universe follows the star formation rate (SFR). The SFR depends on the

redshift z and is given by $\mathcal{H}_{\text{SFR}} \propto (1+z)^{n_i}$, with $n_i = 3.4$ for $z < 1$, $n_i = -0.3$ for $1 < z < 4$ and $n_i = -3.5$ for $z > 4$. The amount of sources at $z = 0$, called the **local density**, is denoted by \mathcal{H}_0 , and expressed in units of inverse volume. Therefore, the amount of neutrino sources \mathcal{H}_{SFR} can be written as a multiplication of this proportionality constant and the dimensionless distribution itself: $\mathcal{H}_{\text{SFR}}(z) = \mathcal{H}_0 \times f_{\text{SFR}}(z)$. The SFR per unit co-moving volume for $\mathcal{H}_0 = 10^{-5} \text{ Mpc}^{-3}$ is shown in figure 4.2.

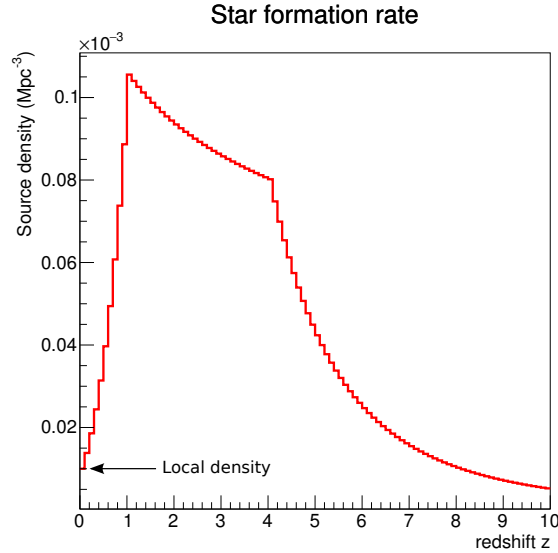


Figure 4.2: Star formation rate (SFR) per unit co-moving volume as a function of redshift z . For this graph, $\mathcal{H}_0 = 10^{-5} \text{ Mpc}^{-3}$.

As the SFR gives a source density, it represents the mathematical quantity of dN/dV_C . We can obtain the number of sources per redshift interval dz by multiplying the SFR by dV_C/dz , which was given in equation 4.4:

$$\frac{dN}{dz} = \frac{dN}{dV_C} \frac{dV_C}{dz} \quad (4.5)$$

$$= \mathcal{H}_{\text{SFR}} 4\pi D_H D_C^2(z) \frac{1}{E(z)} \quad (4.6)$$

This is plotted in figure 4.3. The total amount of neutrino sources N_i in a sphere around the Earth up to z_i can be found by integrating equation 4.6 over dz :

$$N_i = 4\pi D_H \int_0^{z_i} D_C^2(z) \frac{\mathcal{H}_{\text{SFR}}(z)}{E(z)} dz \quad (4.7)$$

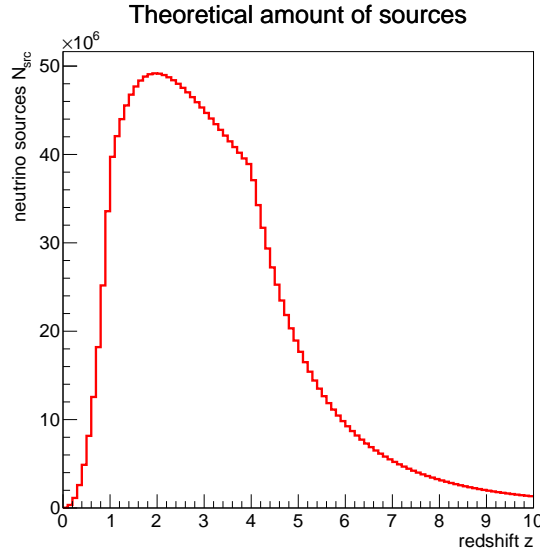


Figure 4.3: Amount of neutrino sources as a function of the redshift. A local source density of $\mathcal{H}_0 = 10^{-5} \text{ Mpc}^{-3}$ has been used. The area under the curve is equal to the total number of sources N_{src} (equation 4.7).

4.3 Neutrino Flux

We make the rough assumption that all neutrino sources in the Universe are identical ‘standard candles’, and therefore emit exactly the same amount of neutrinos in a given time interval. In other words, the **intrinsic neutrino luminosity** L_ν is exactly the same for every source.

The amount of neutrinos we receive on Earth from one source, its **neutrino flux** Φ_ν , is given by

$$\Phi_\nu = \frac{d\Phi}{dN} = \frac{L_\nu}{4\pi D_C^2(z)(1+z)^2} \quad (4.8)$$

where one factor of $(1+z)$ originates from the fact that time is stretched out during the ‘journey’ of the neutrinos, resulting in less neutrinos arriving per second, the other from their lowered energy. The flux is expressed in units of $\text{GeV}^{-1} \text{ s}^{-1} \text{ m}^{-2}$.

The total neutrino flux obtained from all sources in the Universe can be obtained by integrating the total neutrino flux per redshift interval over the redshift z :

$$\Phi_{\text{total}} = \int_0^\infty \frac{d\Phi_{\text{total}}}{dz} dz \quad (4.9)$$

$$= \int_0^\infty \frac{d\Phi}{dN} \frac{dN}{dz} dz = \int_0^\infty \Phi_\nu \frac{dN}{dz} dz \quad (4.10)$$

Since Φ_ν is given by equation 4.8 and dN/dz is given by equation 4.6, we can rewrite equation 4.10 as follows:

$$\Phi_{\text{total}} = \int_0^\infty \frac{L_\nu}{4\pi D_C^2 (1+z)^2} 4\pi D_H D_C^2 \frac{\mathcal{H}_{\text{SFR}}(z)}{E(z)} dz \quad (4.11)$$

Recall that \mathcal{H}_{SFR} can be written as $\mathcal{H}_0 \times f_{\text{SFR}}$, and we can write Φ_{total} as:

$$\Phi_{\text{total}} = \int_0^\infty D_H \mathcal{H}_0 L_\nu \frac{f_{\text{SFR}}(z)}{(1+z)^2 E(z)} dz \quad (4.12)$$

Like Ahlers and Halzen in [3], we now introduce a dimensionless quantity that describes the redshift evolution, ξ :

$$\xi = \int_0^\infty \frac{f_{\text{SFR}}(z)}{(1+z)^2 E(z)} dz \quad (4.13)$$

Since D_H , \mathcal{H}_0 and L_ν in equation 4.12 are all independent of redshift, equation 4.13 allows us to write the total flux as follows:

$$\Phi_{\text{total}} = \xi \mathcal{H}_0 D_H L_\nu \quad (4.14)$$

Since the value for the total flux is known from the IceCube experiment, equation 4.14 enables us to express the neutrino flux per source in terms of the total flux. Substituting $L_\nu = \Phi_{\text{total}} / (\xi \mathcal{H}_0 D_H)$ in equation 4.8, we obtain:

$$\Phi_\nu = \frac{\Phi_{\text{total}}}{4\pi \xi \mathcal{H}_0 D_H D_C^2 (1+z)^2} \quad (4.15)$$

We can also plug equation 4.14 into equation 4.12 and take the derivative with respect to z , to obtain an expression for the amount of flux received from a certain redshift:

$$\begin{aligned} \frac{d\Phi}{dz} &= D_H \mathcal{H}_0 \frac{\Phi_{\text{total}}}{\xi \mathcal{H}_0 D_H} \frac{f_{\text{SFR}}(z)}{(1+z)^2 E(z)} \\ &= \frac{\Phi_{\text{total}}}{\xi} \frac{f_{\text{SFR}}(z)}{(1+z)^2 E(z)} \end{aligned} \quad (4.16)$$

4.4 Simulating a Universe of Neutrino Source Candidates

In the simulation, an entire (isotropic) Universe (up to a user-specified redshift) filled with neutrino sources is generated. The simulation proceeds on an outward shell-by-shell basis, meaning that only one ‘shell’ of co-moving volume is being simulated at a time, starting with the innermost shell.

A shell is defined as the co-moving volume between two values of redshift, z_1 and z_2 . The corresponding co-moving distances D_1 and D_2 of the boundaries are also obtained (using

equation 4.1). Using equation 4.7, we can find the number of sources in the shell N_{shell} between z_1 and z_2 :

$$N_{\text{shell}} = 4\pi D_{\text{H}} \int_{z_1}^{z_2} D_{\text{C}}^2(z) \frac{\mathcal{H}_{\text{SFR}}(z)}{E(z)} dz \quad (4.17)$$

To reduce the run time of the simulation, this has been approximated by taking the centre values of every shell. This is justified because the thickness of the shells $dz (= z_2 - z_1)$ is taken to be very small:

$$N_{\text{shell}} = 4\pi D_{\text{H}} D_{\text{C}}^2(z_{\text{centre}}) \frac{\mathcal{H}_{\text{SFR}}(z_{\text{centre}})}{E(z_{\text{centre}})} dz \quad (4.18)$$

In order to further reduce the run time, the amount of sources to be simulated N_{sim} can be scaled down by dividing N_{shell} by a scalefactor $\mathcal{S}(n) = 10^n$, with $n = 0, 1, 2, \dots$:

$$N_{\text{sim}} = \frac{N_{\text{shell}}}{\mathcal{S}(n)} \quad (4.19)$$

Every generated source in the shell gets a randomly drawn co-moving distance D_{C} between D_1 and D_2 , which is also converted back into a corresponding redshift z . Since the shells have been chosen to be small, we can assume the distribution of D_{C} in the shell to be flat. Additionally, every source gets random right ascension ϕ and declination θ angles, in such a way that the total distribution is isotropic. Lastly, the neutrino flux Φ_{ν} received from every single source is computed using equation 4.15, where for Φ_{total} , the value found by IceCube [1] is used:

$$\Phi_{\text{IceCube}} = 10^{-8} \text{ GeV}^{-1} \text{ s}^{-1} \text{ m}^{-2},$$

where the amount of detected neutrinos that corresponds to this value is a model parameter, which is taken to be $N_{\nu} = 100$. The generated values for $z, \phi, \theta, D_{\text{C}}$ and Φ_{ν} are written to a datafile, after which a new shell can be simulated. This process continues up to a maximum redshift, taken to be $z = 10$. The simulation is carried out for different local densities, ranging from $\mathcal{H}_0 = 10^{-4} \text{ Mpc}^{-3}$ down to $\mathcal{H}_0 = 10^{-9} \text{ Mpc}^{-3}$. The resulting source and flux distributions are plotted and analysed in section 6.

Chapter 5

Simulation of the Expected Signal

To find the optimal detector properties and detection parameters for a given source model, we will first simulate the detected neutrinos. The simulated neutrinos will be plotted in a sky map, together with a given number of source candidates, where the source and flux distributions will follow the ones derived in the previous section. Eventually, however, when analysing real data, the source candidates will be taken from catalogues. Subsequently, the signal will be compared to the sources. Our test statistic, the number of hits, is defined as the amount of neutrinos that are within a certain angular distance from a source, and computed for both the background-only and background plus signal scenarios. The distribution of the number of hits will then be used in an analytical analysis to compute the significance of the signal, and test different detection parameters.

5.1 Sky Maps

For a given amount of sources in our catalogue (i.e. the *catalogue size*) N_{src} and a given local source density \mathcal{H}_0 , we can compute the fraction that these sources together contribute to the total flux (assuming the catalogue is perfect), by using the relation plotted in figure 5.1. We call this fraction the **flux fraction** f_Φ . If, for instance, we take $\mathcal{H}_0 = 10^{-9}$ and $N_{\text{src}} = 4000$, we obtain $f_\Phi \approx 0.80$. As a consequence, this means that for objects with this local source density, 80% of the neutrinos should come from the 4000 brightest (and therefore closest) neutrino sources, whereas the other 20% should be coming from sources further away.

If, however, our neutrino signal does not come from the current source candidate, we expect the signal to be isotropically distributed. Therefore, the **neutrino correlation fraction** f_ν can take up two values: $f_\nu = f_\Phi$ or $f_\nu = 0$. Combined with the amount of detected neutrinos N_ν , we can obtain the amounts of correlated and random neutrinos, $N_{\nu,c}$ and $N_{\nu,r}$,

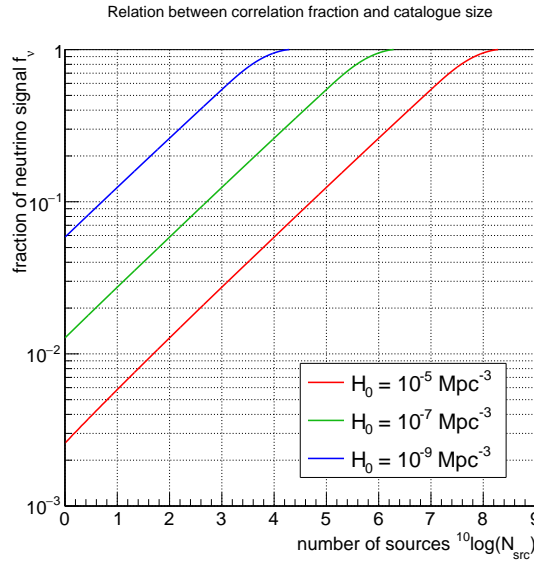


Figure 5.1: Relation between the neutrino correlation fraction (or flux fraction) and the number of sources included in the analysis, for different local sources densities. See equations 4.7 and 4.12 for a mathematical relation.

respectively:

$$N_{\nu,c} = f_\nu N_\nu \quad (5.1)$$

$$N_{\nu,r} = (1 - f_\nu) N_\nu = N_\nu - N_{\nu,c} \quad (5.2)$$

The simulation of the expected signal starts by isotropically generating coordinates for N_{src} sources and $N_{\nu,r}$ neutrinos. As mentioned in the previous section, as a benchmark, we take N_ν to be 100. After generation, the sources and random neutrinos are plotted in a sky map as blue dots and red crosses, respectively. Subsequently, coordinates for all correlated neutrinos are generated around randomly picked sources, with the angular distance between the neutrino and its corresponding source picked from a Gaussian distribution. The standard deviation of this distribution is related to the **angular resolution** ψ of the detector as $\sigma(\psi) = \psi / \sqrt{2 \ln 2}$. After this, the $N_{\nu,c}$ neutrinos that come from sources included in the catalogue are plotted in the sky map as red crosses as well (see figure 5.2).

5.2 Counting Hits

Now, for a given sky map, we seek to match the neutrino signal to the sources in the sky map. The **amount of hits** N_{hits} is computed by counting the amount of neutrinos that are within a **search cone** with angular radius β from a source. If we now repeat this process multiple times, we are able to fill a histogram (see figure 5.3) with the obtained values for N_{hits} .

The total amount of hits can be divided into two components: random hits and signal hits. Random hits are the hits that occur by chance, even when there is no correlation ($f_\nu = 0$).

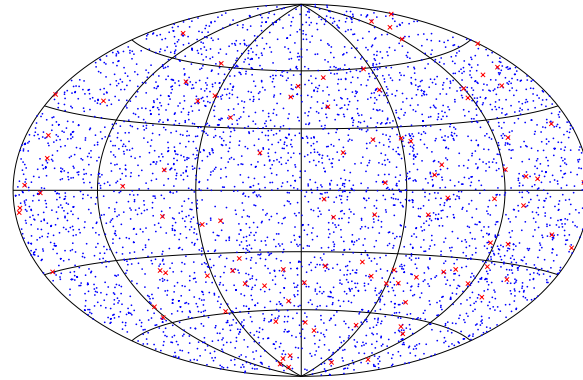


Figure 5.2: A simulated sky map. Sources are represented as blue dots, neutrinos as red crosses.

The amount of random hits $N_{\text{hits, random}}$ increases with increasing amounts of both neutrinos and sources, as well as the radius of the search cone, and is Poisson-distributed. Signal hits are hits due to the correlation between neutrinos and sources. The amount of signal hits $N_{\text{hits, signal}}$ should increase for an increased amount of neutrinos and for an increased correlation factor.

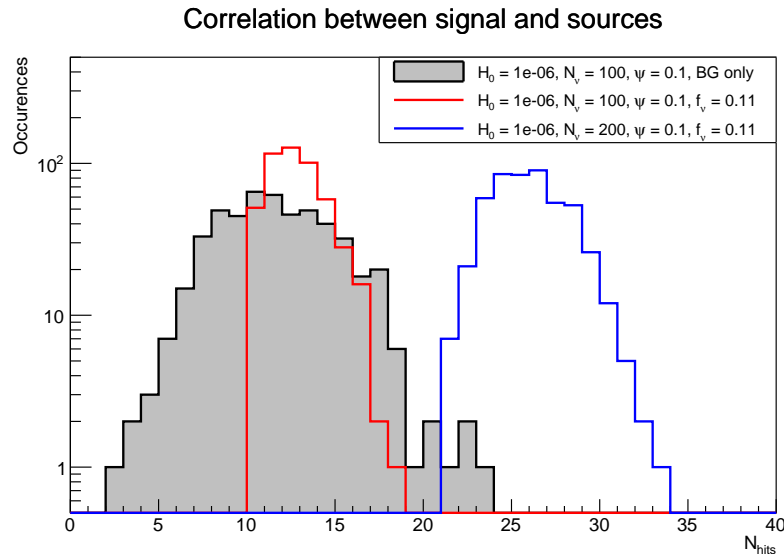


Figure 5.3: Correlation between a neutrino signal and sources. The grey shaded area is the distribution of background hits for $\mathcal{H}_0 = 10^{-6} \text{ Mpc}^{-3}$, $N_\nu = 100$ and $\psi = 0.1^\circ$. The red line shows the distribution for the same set of detector parameters, but includes signal hits as well. The correlation fraction of $f_\nu = 0.11$ results in enough signal hits to increase the mean of the distribution. The blue line represents the same distribution as the red line, but with double the amount of neutrinos, leading to a large increase in the mean number of hits.

5.3 Confidence Levels

The distribution of N_{hits} follows a Poisson distribution, where the mean of the background distribution ($f_\nu = 0$) is equal to the expected amount of random hits:

$$N_{\text{hits, random}} = N_\nu N_{\text{src}} \frac{\Omega_{\text{cone}}}{4\pi} = N_\nu N_{\text{src}} \frac{1 - \cos \beta}{2} \quad (5.3)$$

Now, the mean of the distribution with correlated neutrinos ($f_\nu = f_\Phi$) is approximately equal to the sum of the expected amount of random hits and the expected amount of signal hits:

$$N_{\text{hits, total}} = N_{\text{hits, random}} + N_{\text{hits, signal}}, \quad (5.4)$$

where the expected amount of signal hits depends on f_ν , N_ν and the **cone efficiency** ϵ :

$$N_{\text{hits, signal}} = f_\nu N_\nu \epsilon(\psi, \beta) \quad (5.5)$$

The neutrino correlation fraction f_ν can be computed for a given local source density \mathcal{H}_0 and amount of observed sources N_{src} , using the relation plotted in figure 5.1. The detector efficiency $\epsilon(\psi, \beta)$ is given by

$$\epsilon(\psi, \beta) = 1 - \exp\left(-\ln(2) \frac{\beta^2}{\psi^2}\right) \quad (5.6)$$

Using Poisson statistics, p -values can be computed for given values of \mathcal{H}_0 , N_{src} , N_ν , ψ and β . Subsequently, for given values of \mathcal{H}_0 , N_ν , ψ and β , the value for N_{src} that gives the best significance can be computed. By converting the obtained p -values, the confidence levels (CLs) will eventually be expressed in sigmas.

Chapter 6

Analysis

In this section, the source distributions and corresponding flux distributions will be analysed. The detector response for different detector parameters will be computed and plotted for different source candidates. Eventually, the maximum confidence level for all parameter settings will be extracted.

6.1 Source Distribution

The simulated amount of sources per redshift interval for a local source density of 10^{-5} Mpc^{-3} is plotted as a function of the redshift z in figure 6.1, with a theoretical curve for dN/dz (equation 4.6, figure 4.3) plotted on top.

As shown in the graph, there are relatively few sources for redshifts $z \ll 1$. This is due to both the low star formation rate for these redshifts (see figure 4.2) and the fact that the co-moving volume is still relatively small. The amount of sources then rapidly increases with z , until it reaches its maximum at $z = 2.0$. At $z = 4$, it starts to drop exponentially, thanks to the SFR, leading to a relatively low amount of sources at higher redshift. When integrating figure 6.1 over redshift, we obtain the curves shown in figure 6.2, which provide us with an enhanced insight in the relative source distribution.

As can be seen in the graphs mentioned above, the total amount of sources becomes approximately constant at $z = 5$, meaning that nearly all of the sources are located at $z \leq 5$. Clearly, the shape of the distribution is independent of local source density, but the amount of sources is not.

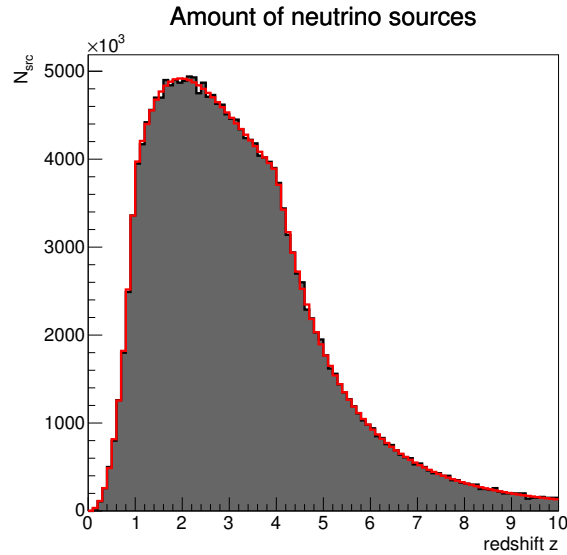


Figure 6.1: Amount of neutrino sources per redshift interval, as a function of the redshift. The black bins show the simulated sources, the red curve is the amount of sources that we expect from theory. For this graph, the local density equals $\mathcal{H}_0 = 10^{-5} \text{ Mpc}^{-3}$.

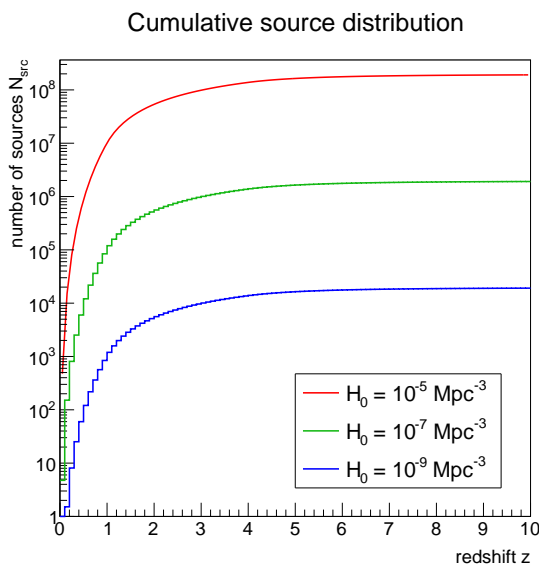


Figure 6.2: Integrated amount of sources versus redshift, for local source densities of 10^{-5} (red), 10^{-7} (green) and 10^{-9} (blue) Mpc^{-3} .

6.2 Flux Distribution

Since the flux of a source depends on the local source density \mathcal{H}_0 (because all sources together must account for the observed total flux), the redshift z and several constants (see equation 4.15), the amount of sources that have a given neutrino flux is, in contrast to the source distribution, expected to differ for various local densities. As the total flux Φ_{total} is constant, the existence of more sources implies a lower neutrino flux per source. Therefore, an *observed* amount of sources with a given flux could give insight into the actual value of \mathcal{H}_0 .

Figure 6.3 shows the yearly neutrino event distribution for various values of \mathcal{H}_0 , where the amount of detected neutrinos that corresponds to the total flux is a model parameter, here taken to be $N_\nu = 100$. As expected, the most frequent flux value ‘moves’ one order of magnitude to the left when the local source density increases one order of magnitude. This is due to the fact that the total flux has to be distributed amongst more sources, leading to a lower flux per source. Furthermore, the peak increases by one order of magnitude, due to the increased local source density. This way, the integral of the histogram is constant under varying local source densities.

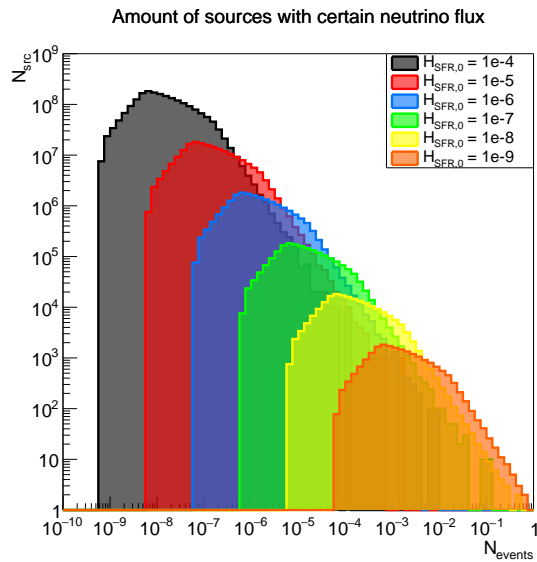


Figure 6.3: Amount of sources with a certain amount of yearly detected neutrinos for $\mathcal{H}_0 = 10^{-4}$ (black), 10^{-5} (red), 10^{-6} (blue), 10^{-7} (green), 10^{-8} (yellow) and 10^{-9} (orange) Mpc^{-3} . It has been assumed that the IceCube flux Φ_{IceCube} corresponds to 100 detected neutrino events per year.

The flux-weighted redshift distribution, however, is constant under a varying local source density. In figure 6.4, the flux distribution has been plotted as a function of redshift. For different values of \mathcal{H}_0 , the flux per source would vary, but the total flux provided by sources from a given redshift would not, as this would be compensated by the different amount of sources. The integral of the plot again gives Φ_{total} .

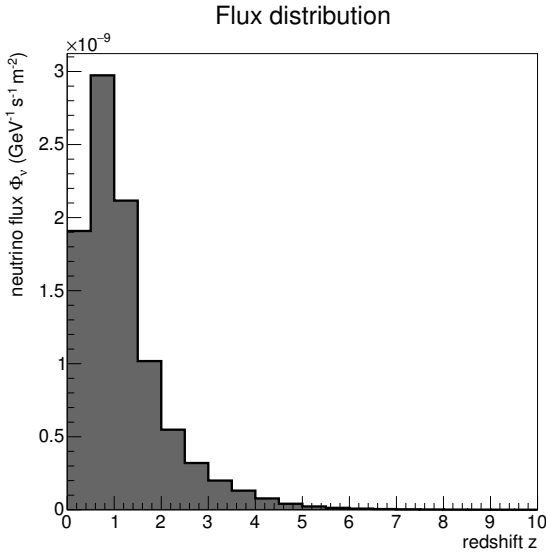


Figure 6.4: The total received flux, as a function of redshift. Integrating gives Φ_{total} . The distribution is constant under varying local density: The flux per source would differ, but so would the amount of sources, leading to the exact same flux coming from a given redshift interval.

Clearly, the largest part of the flux comes from sources at $z \leq 2$. The main cause for this is that the flux is inversely proportional to the square of both the redshift and the co-moving distance (again, see equation 4.15). Furthermore, as can be deduced from figure 6.2, approximately 80% of the sources is located in the same redshift range, leading to a further suppression of flux from high-redshift sources. The same can be concluded from figure 5.1.

If we now integrate figure 6.4 over z , we obtain the flux fraction f_Φ as a function of redshift, plotted in figure 6.5. Like in figure 6.2, the cumulative distribution becomes approximately constant for $z > 5$, again confirming that sources further away are relatively weak and do not significantly contribute to the total flux. Combined with the findings from the previous section, this implies that sources further away than $z = 5$ can be almost neglected in the analysis. Moreover, the distribution is independent of the local density.

6.3 Benchmark Significance

As a benchmark model for our detector, $N_\nu = 100$ detected neutrinos and an angular resolution of $\psi = 0.1^\circ$ have been assumed. As mentioned in section 2.3, the local source densities of blazars, hard X-ray emitting AGN and starburst galaxies are taken to be $\mathcal{H}_0 = 10^{-9}$, 10^{-6} and 10^{-4} Mpc^{-3} , respectively. We compute the amount of random and signal hits and compute the significance of the latter using the methods described in chapter 5. This has been done for different values of N_{src} , optimising the search cone radius β for every set of parameters, thereby reducing the amount of input parameters. The optimal settings for the

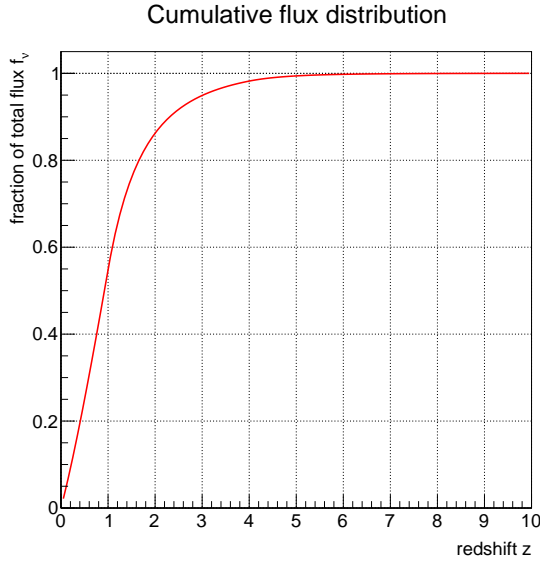


Figure 6.5: Cumulative flux distribution. The red curve indicates the fraction of the total flux Φ_{total} provided by all sources up to a given redshift.

benchmark detector are shown for three local densities - the values of which are roughly equal to the local densities of blazars, AGN and starburst galaxies - in table 6.1.

It turns out that, for the assumed parameters, sources with local densities up to 10^{-9} Mpc^{-3} can be discovered at 5σ significance. For sources with a higher local density, however, this is not the case. To achieve the same significance for these more abundant sources, the benchmark model should be improved. Potential improvements are a higher acceptance, a smaller resolution, or both. The effects of these potential improvements on the significance are explored in the next section.

Class of source	$\mathcal{H}_0 (\text{Mpc}^{-3})$	N_ν	$\psi (\text{°})$	$\beta (\text{°})$	f_ν	N_{src}	CL (σ)
Blazars	10^{-9}	100	0.1	0.1901	0.8184	4170	22.13
AGN	10^{-6}	100	0.1	0.1671	0.1015	5376	5.009
Starburst Galaxies	10^{-4}	100	0.1	0.1658	0.0166	2226	1.656

Table 6.1: Maximum confidence levels for the benchmark detector ($N_\nu = 100$, $\psi = 0.1^\circ$). For both blazars and AGN, the confidence level is high enough to speak of a ‘discovery’. For starburst galaxies, however, this is not the case.

6.4 Different Detector Models

To study the impact of the detector resolution and the acceptance, the performance of four ‘detector models’ has been mapped out: the benchmark model, with $N_\nu = 100$ and $\psi = 0.1^\circ$, a model with a decreased resolution ($\psi = 0.5^\circ$), a model with a higher acceptance ($N_\nu = 500$), and one with both a decreased resolution and higher acceptance.

For each of these detector models, the confidence level has been computed for different values of N_{src} , optimising β for every parameter set. The confidence levels for blazars, AGN and starburst galaxies are plotted as a function of N_{src} in figures 6.6, 6.7 and 6.8, respectively. In each figure, the benchmark model is represented by a black solid line, the lines of the models with an increased acceptance are red, and the models with a larger resolution have dashed lines.

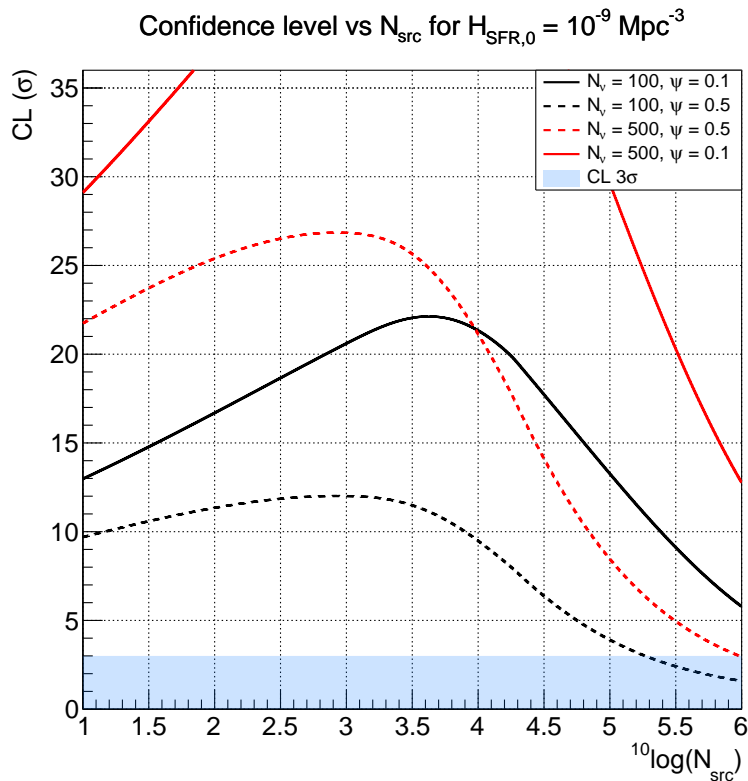


Figure 6.6: Confidence levels for a local density of $\mathcal{H}_0 = 10^{-9} \text{ Mpc}^{-3}$ (blazars) and different detector settings. The solid black line is the benchmark model, which has a resolution of 0.1° and an acceptance of 100ν . The dashed lines have a larger resolution (0.5°), whereas a red colour indicates an increased acceptance (500ν). Confidence levels lower than 3σ are within the blue shaded area. Evidently, all lines reach confidence levels much larger than 3σ . See table 6.2 for the maximum significance values and the corresponding detection parameters.

In figure 6.6, it can be seen that increasing the acceptance (red solid line) greatly improves the maximum confidence level (see table 6.2 for the maximum values and the corresponding detection parameters). Furthermore, having a larger resolution (black dashed line) has a negative effect on the significance. However, when compensating the larger resolution with an increased acceptance (red dashed line), the maximum confidence level surpasses that of the benchmark model. Moreover, for this larger resolution, the amount of sources required to achieve the maximum significance goes down. This can be explained by the fact that for a worse resolution, the amount of random hits will be relatively higher. The impact of these background hits can be suppressed by incorporating a lower amount of sources in the analysis. This works both ways: for a smaller resolution, more sources are required for the maximum confidence level. The values in table 6.2 support this explanation.

N_ν	ψ (°)	β (°)	f_ν	N_{src}	$N_{\text{hits, random}}$	$N_{\text{hits, signal}}$	CL (σ)
100	0.1	0.190	0.8194	4193	1.154	75.243	22.128
100	0.5	0.844	0.5198	856	4.646	44.777	12.011
500	0.5	0.844	0.5160	837	22.701	222.25	26.849
500	0.1	0.211	0.2680	108	0.182	127.85	> 36

Table 6.2: Maximum confidence levels for $\mathcal{H}_0 = 10^{-9}$ Mpc $^{-3}$ (blazars), for the four different detector models. Since the model with both the best resolution and best acceptance achieves a confidence level of $\text{CL} \geq 36\sigma$ for a wide range of N_{src} , the settings for the smallest catalogue size that gives $\geq 36\sigma$ are shown.

In the case of AGN, shown in figure 6.7, again, the significance greatly increases for an improved acceptance. For a worse resolution, the maximum confidence level is lowered again as well, but this time, it drops below 3σ . When compensating this resolution with a higher acceptance, the significance is approximately equal again to the maximum significance for the benchmark model. The optimal settings for every set of detector parameters are denoted in table 6.3. When comparing these values to those of the previous scenario, we can observe that the optimal values of the correlation fraction f_ν are lower. This is due to the fact that for AGN, a higher local density has been assumed, meaning there are more sources. Therefore, an equal correlation fraction would result in a very high amount of sources, which would in turn lead to a relatively large amount of background hits. This effect can be partially mitigated by choosing a low correlation fraction. A lower value of f_ν implies a reduced background, but also fewer neutrinos correlating to the selected sources.

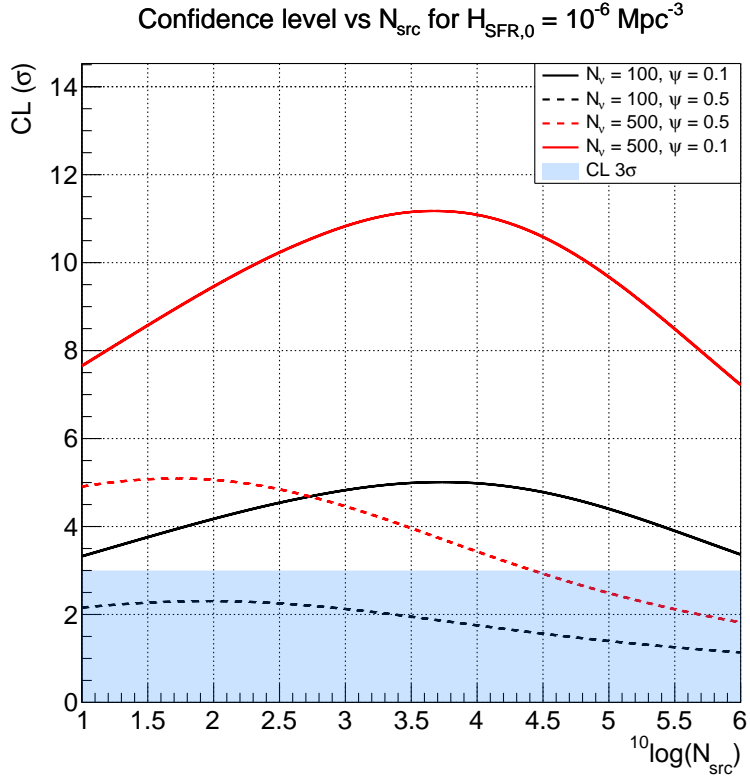


Figure 6.7: Confidence levels for a local density of $\mathcal{H}_0 = 10^{-6} \text{ Mpc}^{-3}$ (AGN) and different detector settings. See table 6.3 for the maximum significance values and the corresponding detection parameters.

N_ν	ψ (°)	β (°)	f_ν	N_{src}	$N_{\text{hits, random}}$	$N_{\text{hits, signal}}$	CL (σ)
100	0.1	0.167	0.1017	5401	1.148	8.698	5.009
100	0.5	0.832	0.0263	88	0.462	2.241	2.304
500	0.5	0.831	0.0219	50	1.325	9.322	5.093
500	0.1	0.167	0.0968	4651	4.950	41.435	11.175

Table 6.3: Maximum confidence levels for $\mathcal{H}_0 = 10^{-6} \text{ Mpc}^{-3}$ (AGN), for the four different detector models.

As expected, an increased acceptance increases the maximum significance for starburst galaxies as well. As becomes clear from figure 6.8, however, this is the *only* model out of the four detector models that exceed the 3σ region. In table 6.4, we can see that for the detector model with the lowest maximum confidence level ($N_\nu = 100, \psi = 0.5^\circ$), the amount of random hits is higher than the amount of signal hits, resulting in a significance as low as 0.891σ . When compensated by a larger acceptance, the maximum significance is again approximately equal to that of the benchmark model. To achieve this, a very small correlation fraction (and therefore amount of sources) is chosen, thereby bringing down the amount of background hits.

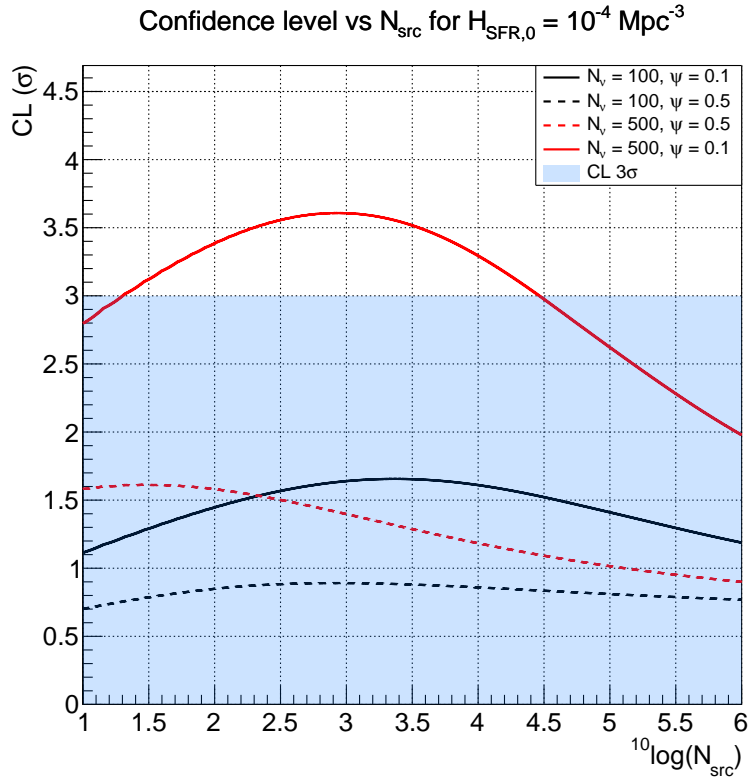


Figure 6.8: Confidence levels for a local density of $\mathcal{H}_0 = 10^{-4} \text{ Mpc}^{-3}$ (starburst galaxies) and different detector settings. See table 6.4 for the maximum significance values and the corresponding detection parameters.

N_ν	ψ (°)	β (°)	f_ν	N_{src}	$N_{\text{hits, random}}$	$N_{\text{hits, signal}}$	CL (σ)
100	0.1	0.167	0.0166	2226	0.466	1.418	1.656
100	0.5	0.826	0.0119	818	4.243	1.011	0.891
500	0.5	0.812	0.0038	29	0.728	1.592	1.614
500	0.1	0.165	0.0119	818	0.851	5.058	3.608

Table 6.4: Maximum confidence levels for $\mathcal{H}_0 = 10^{-4} \text{ Mpc}^{-3}$ (starburst galaxies), for the four different detector models.

Chapter 7

Conclusions and Outlook

Since several assumptions were made during this research, it can (and should) be improved by future studies.

To begin with, it has been assumed that the source distributions of all source candidates are proportional to the star formation rate, which is not necessarily true. Other source evolution functions should be included when addressing particular source types to improve the accuracy of the analysis.

Moreover, all sources have been assumed to be ‘standard candles’: objects of equal luminosity. This simplifies the analysis, since it allows us to easily compute the neutrino flux we expect to receive from a given source, whilst ensuring the flux of all sources together adds up to the total flux. However, sources of a given type can be vastly different in luminosity. Future studies could incorporate the effects of these differences in the analysis.

Furthermore, the catalogues of source candidates considered in this research have been assumed to be ‘perfect’: catalogues that include every source of a given type present in the Universe, again following the star formation rate. Since real-life catalogues are usually not ‘perfect’, the actual confidence levels are expected to go down, because the sources in the catalogue could provide a smaller fraction of the total flux than expected. This issue could possibly be avoided by doing follow-up (electromagnetic) measurements of each neutrino event.

Finally, the assumed amounts of 100 and 500 detected cosmic neutrinos are realistic numbers, but it would take several years to detect these amounts (with the currently planned effective area).

7.1 Conclusions

The analysis presented in the previous section allow us to draw a number of conclusions, which in turn provide us with answers to the main questions of this research project: what are the roles of the pointing resolution and the acceptance, and are we able to test the hypotheses on cosmic neutrino source candidates? Another goal of this research was to understand how to integrate the flux contributions of individual sources over a volume in the Universe.

The most important outcome of this research is that a small resolution is a hard requirement to achieve high confidence levels, especially for source candidates that typically have larger local densities, such as hard X-ray emitting AGN and starburst galaxies. For these objects, a larger resolution means that the expected significance, even with the idealised detector and perfect catalogue that we have assumed, is below 3σ . For source candidates with smaller local densities, such as blazars, the effect is not as strong as in the large local density-case, but it decreases the maximum significance nonetheless. However, since the small resolution for muon neutrinos ($\psi = 0.1^\circ$) will be a key feature of KM3NeT, this should not pose any problems.

However, another major conclusion is that for larger local densities, a worse resolution can be compensated by a larger acceptance. The calculations carried out in this research show that a five times worse resolution, but five times better acceptance results in approximately the same maximum significance: $\text{CL}_{\max}(\alpha N_\nu, \alpha\psi) \approx \text{CL}_{\max}(N_\nu, \psi)$. For smaller local densities, it even results in higher maximum confidence levels.

The obtained values for the maximum confidence levels are sufficiently high to test hypotheses on the sources of cosmic neutrinos. If we collect data until we have detected 500 cosmic neutrinos, and these sources have a local density of $\mathcal{H}_0 = 10^{-4} \text{ Mpc}^{-3}$ (e.g. starburst galaxies), we should be able to determine them with a significance of 3.6σ . For sources candidates with smaller local densities (such as blazars and AGN), the significance gets even higher. For these source candidates, the detection of 100 cosmic neutrinos should already be sufficient to achieve confidence levels above 5σ . It should be noted, however, that the effects of atmospheric neutrinos have not been taken into account in this research. Doing so would increase the amount of background hits, leading to lower confidence levels.

Another conclusion that can be drawn from this research is that if the pointing resolution of the detector is increased, more potential sources have to be included in the analysis. Consequently, larger source catalogues ($N_{\text{src}} \sim 5000$) are required.

Bibliography

- [1] M. G. Aartsen et al. Evidence for High-Energy Extraterrestrial Neutrinos at the IceCube Detector. *Science*, 342:1242856, 2013.
- [2] I. Bartos, M. Ahrens, C. Finley, and S. Marka. Prospects of Establishing the Origin of Cosmic Neutrinos using Source Catalogs. 2016.
- [3] Markus Ahlers and Francis Halzen. Pinpointing Extragalactic Neutrino Sources in Light of Recent IceCube Observations. *Phys. Rev.*, D90(4):043005, 2014.
- [4] Kohta Murase and Eli Waxman. Constraining High-Energy Cosmic Neutrino Sources: Implications and Prospects. *Phys. Rev.*, D94(10):103006, 2016.
- [5] L. M. Brown. The idea of the neutrino. *Physics Today*, 31:23–28, September 1978.
- [6] A. Das and T. Ferbel. *Introduction to Nuclear and Particle Physics*. J. Wiley, 1994.
- [7] The University of Reading. PHYS 9.2: Radioactive decay, 1996.
- [8] C. L. Cowan, Jr., F. Reines, F. B. Harrison, H. W. Kruse, and A. D. McGuire. Detection of the Free Neutrino: A Confirmation. *Science*, 124:103–104, July 1956.
- [9] M. Thomson. *Modern Particle Physics*. Cambridge University Press, 2013.
- [10] The ATLAS Collaboration. Observation of a new particle in the search for the Standard Model Higgs boson with the ATLAS detector at the LHC. *Phys. Lett.*, B716:1–29, 2012.
- [11] The CMS Collaboration. Observation of a new boson at a mass of 125 GeV with the CMS experiment at the LHC. *Phys. Lett.*, B716:30–61, 2012.
- [12] Chandra X ray Observatory. Field Guide to X-ray Sources: Starburst Galaxies, 2012.
- [13] Markus Ahlers and Francis Halzen. High-energy cosmic neutrino puzzle: a review. *Rept. Prog. Phys.*, 78(12):126901, 2015.
- [14] NASA. The Antennae Galaxies/NGC 4038-4039, 2006.
- [15] L. Bergstrom and A. Goobar. *Cosmology and Particle Astrophysics*. Wiley-Praxis Series in Astronomy & Astrophysics. Wiley, 1999.

- [16] M. Ajello et al. The Cosmic Evolution of Fermi BL Lacertae Objects. *Astrophys. J.*, 780:73, 2014.
- [17] The KM3NeT Collaboration. KM3NeT website, 2017.
- [18] Annarita Margiotta. The KM3NeT deep-sea neutrino telescope. *Nucl. Instrum. Meth.*, A766:83–87, 2014.
- [19] S. Adrian-Martinez et al. Letter of intent for KM3NeT 2.0. *J. Phys.*, G43(8):084001, 2016.
- [20] The KM3NeT Collaboration. KM3NeT Astroparticle Oscillations Research with Cosmics in the Abyss Strategy Report, 2015.
- [21] Franco Ferrari and Ewa Szuszkiewicz. Cosmic ray recipes. 2006.
- [22] Daniel Fokkema. *The HISPARC Cosmic Ray Experiment - Data Acquisition and Reconstruction of Shower Direction*. PhD thesis, Universiteit Twente, 2012.
- [23] Claus Grupen. *Astroparticle Physics*. Springer, 2005.
- [24] M. Circella, P. Coyle, and P. Kooijman. The Digital Optical Module -DOM- of the KM3NeT detector. In *Proceedings, 33rd International Cosmic Ray Conference (ICRC2013): Rio de Janeiro, Brazil, July 2-9, 2013*, page 1223.
- [25] Hamamatsu. *Photomultiplier tubes - Basics and Applications*. Hamamatsu, 3a edition, 2007.
- [26] David W. Hogg. Distance measures in cosmology. 1999.
- [27] B.S. Ryden. *Introduction to Cosmology*. Addison-Wesley, 2003.

List of Figures

2.1	For a two-body decay, all observed electrons are expected to have the same energy $T_e = \Delta m c^2$ (the red line). The black curve shows the observed spectrum. Note that the amount of electrons converges to zero at $T_e = T_{\max} = \Delta m c^2$. Figure originally taken from [7].	5
2.2	Summary of all fundamental particles in the Standard Model. The first three columns contain the fermions, particles with half-integer spin. The quarks are in purple, the leptons in green. The fourth column lists the gauge bosons, particles with integer spin that act as mediators of the fundamental interactions. On the top right in yellow is the Higgs boson, which provides the mechanism by which particles acquire mass.	6
2.3	Graphical overview of the interactions in the Standard Model. The interactions are indicated by blue lines, the elementary particles by the black dots. As shown, the gluon only interacts with the colour-carrying quarks, the photon couples to all quarks, the charged leptons and W^\pm boson, the weak gauge bosons to all quarks and leptons and the Higgs boson to all particles that have mass, including itself. Note that this graph assumes the neutrinos to be massless (and therefore assumes that there exist no interactions between neutrinos and the Higgs boson).	7
2.4	The Antennae Galaxies (NGC 4038 and NGC 4039), two interacting galaxies currently going through a starburst phase. The collision of the two galaxies causes a very high star formation [14].	8
2.5	Image of a galaxy with an active galactic nucleus. The nucleus, a (super)massive black hole (shown in red), accretes matter from the galaxy (grey disk), producing relativistic jets of particles in the process (dark blue). The accretion process causes shock fronts (light blue) as well, accelerating the particles in the jets. These particles interact with other particles and form pions, which eventually decay to neutrinos during flight.	9
3.1	Map of the Mediterranean Sea showing the locations of the three KM3NeT sites: Toulon (France), Capo Passero (Italy) and Pylos (Greece) [18].	11

3.2 Schematic of the main interactions of cosmic rays in the Earth's atmosphere. Protons enter the atmosphere and collide with atmosphere molecules. The main products of these interactions are pions, neutrons and protons. The neutral pions decay to two photons, starting an electromagnetic cascade of photons and electrons. The charged pions, on the other hand, will decay to (anti)muons and their corresponding (anti)neutrinos.	13
3.3 Schematic of Cherenkov radiation. An incoming charged particle, depicted by the red arrow, traverses a dielectric medium with refractive index n at velocity $v = \beta c$. If $\beta > \frac{1}{n}$, constructive interference will occur and Cherenkov radiation will be emitted (blue arrows).	14
3.4 Schematic overview of a KM3NeT building block [17].	15
3.5 Photograph of a Digital Optical Module (DOM). The yellow disks are the faces of the photomultiplier tubes [19].	16
3.6 Illustration of a photomultiplier tube (PMT). On the left, photons strike the photocathode, producing electrons. The electrons are directed to the dynodes using an electric field. At every dynode, the amount of electrons is multiplied. Eventually, the electrons are collected at the anode, where they induce a current [25].	16
4.1 Graph showing the co-moving distance D_C corresponding to a redshift z . Redshift is a dimensionless quantity, co-moving distance is given in Gpc.	18
4.2 Star formation rate (SFR) per unit co-moving volume as a function of redshift z . For this graph, $\mathcal{H}_0 = 10^{-5} \text{ Mpc}^{-3}$	19
4.3 Amount of neutrino sources as a function of the redshift. A local source density of $\mathcal{H}_0 = 10^{-5} \text{ Mpc}^{-3}$ has been used. The area under the curve is equal to the total number of sources N_{src} (equation 4.7).	20
5.1 Relation between the neutrino correlation fraction (or flux fraction) and the number of sources included in the analysis, for different local sources densities. See equations 4.7 and 4.12 for a mathematical relation.	24
5.2 A simulated sky map. Sources are represented as blue dots, neutrinos as red crosses.	25
5.3 Correlation between a neutrino signal and sources. The grey shaded area is the distribution of background hits for $\mathcal{H}_0 = 10^{-6} \text{ Mpc}^{-3}$, $N_\nu = 100$ and $\psi = 0.1^\circ$. The red line shows the distribution for the same set of detector parameters, but includes signal hits as well. The correlation fraction of $f_\nu = 0.11$ results in enough signal hits to increase the mean of the distribution. The blue line represents the same distribution as the red line, but with double the amount of neutrinos, leading to a large increase in the mean number of hits.	25

6.1	Amount of neutrino sources per redshift interval, as a function of the redshift. The black bins show the simulated sources, the red curve is the amount of sources that we expect from theory. For this graph, the local density equals $\mathcal{H}_0 = 10^{-5} \text{ Mpc}^{-3}$	28
6.2	Integrated amount of sources versus redshift, for local source densities of 10^{-5} (red), 10^{-7} (green) and 10^{-9} (blue) Mpc^{-3}	28
6.3	Amount of sources with a certain amount of yearly detected neutrinos for $\mathcal{H}_0 = 10^{-4}$ (black), 10^{-5} (red), 10^{-6} (blue), 10^{-7} (green), 10^{-8} (yellow) and 10^{-9} (orange) Mpc^{-3} . It has been assumed that the IceCube flux Φ_{IceCube} corresponds to 100 detected neutrino events per year.	29
6.4	The total received flux, as a function of redshift. Integrating gives Φ_{total} . The distribution is constant under varying local density: The flux per source would differ, but so would the amount of sources, leading to the exact same flux coming from a given redshift interval.	30
6.5	Cumulative flux distribution. The red curve indicates the fraction of the total flux Φ_{total} provided by all sources up to a given redshift.	31
6.6	Confidence levels for a local density of $\mathcal{H}_0 = 10^{-9} \text{ Mpc}^{-3}$ (blazars) and different detector settings. The solid black line is the benchmark model, which has a resolution of 0.1° and an acceptance of 100 ν . The dashed lines have a larger resolution (0.5°), whereas a red colour indicates an increased acceptance (500 ν). Confidence levels lower than 3σ are within the blue shaded area. Evidently, all lines reach confidence levels much larger than 3σ . See table 6.2 for the maximum significance values and the corresponding detection parameters. . .	32
6.7	Confidence levels for a local density of $\mathcal{H}_0 = 10^{-6} \text{ Mpc}^{-3}$ (AGN) and different detector settings. See table 6.3 for the maximum significance values and the corresponding detection parameters.	34
6.8	Confidence levels for a local density of $\mathcal{H}_0 = 10^{-4} \text{ Mpc}^{-3}$ (starburst galaxies) and different detector settings. See table 6.4 for the maximum significance values and the corresponding detection parameters.	35

List of Tables

2.1	Typical - but approximate - numbers for the local source densities of the different source candidates considered in this project: starburst galaxies, hard X-ray emitting AGN and blazars [3; 4; 2].	10
6.1	Maximum confidence levels for the benchmark detector ($N_\nu = 100$, $\psi = 0.1^\circ$). For both blazars and AGN, the confidence level is high enough to speak of a ‘discovery’. For starburst galaxies, however, this is not the case.	31
6.2	Maximum confidence levels for $\mathcal{H}_0 = 10^{-9} \text{ Mpc}^{-3}$ (blazars), for the four different detector models. Since the model with both the best resolution and best acceptance achieves a confidence level of $\text{CL} \geq 36\sigma$ for a wide range of N_{src} , the settings for the smallest catalogue size that gives $\geq 36\sigma$ are shown.	33
6.3	Maximum confidence levels for $\mathcal{H}_0 = 10^{-6} \text{ Mpc}^{-3}$ (AGN), for the four different detector models.	34
6.4	Maximum confidence levels for $\mathcal{H}_0 = 10^{-4} \text{ Mpc}^{-3}$ (starburst galaxies), for the four different detector models.	35

Acknowledgements

After almost a year, I would like to thank the people who, each in their own way, contributed to my project and thesis.

First of all, I would like to thank Aart Heijboer, for his enthusiastic supervision and support in the past eleven months. He continuously provided me with feedback and new challenging ideas to work out, which greatly motivated me. This made the project both entertaining and instructive.

Secondly, I would like to express my gratitude to the entire KM3NeT group at Nikhef for making me feel part of the team from the very first day, the highlight of which being the Collaboration Meeting in Bari. Special thanks go out to Martijn Jongen, for helping me out with the theoretical part of my thesis.

Furthermore, I would like to thank Shin'ichiro Ando for not only being the second examiner of my project, but for giving me helpful feedback on my thesis as well.

I would like to thank Lotte, Marloes and my parents for providing a listening ear for my frequent trains of thought, and their never-ending support.

I also wish to give a shout-out to Wesley, Stephan, Joran, and especially Bram, who managed to survive in a room with me for ten months. Our (sometimes extensive) tea and table tennis breaks helped to highly enhance the atmosphere.

Finally, I would like to thank everyone who took the time to attend my presentation at Nikhef.